Check for updates

Inverse design and demonstration of high-performance wide-angle diffractive optical elements

DONG CHEON KIM,[1,*] (ID) ANDREAS HERMERSCHMIDT,[2] PAVEL DYACHENKO,[2] AND TORALF SCHARF[1] (ID)

[1]*Nanophotonics and Metrology Laboratory (NAM), EPFL, 1015 Lausanne, Switzerland*
[2]*Holoeye Photonics AG, 12489 Berlin, Germany*
*dong.kim@epfl.ch

Abstract: Diffractive optical elements are ultra-thin optical components required for constructing very compact optical 3D sensors. However, the required wide-angle diffractive 2D fan-out gratings have been elusive due to design challenges. Here, we introduce a new strategy for optimizing such high-performance and wide-angle diffractive optical elements, offering unprecedented control over the power distribution among the desired diffraction orders with only low requirements with respect to computational power. The microstructure surfaces were designed by an iterative gradient optimization procedure based on an adjoint-state method, capable to account for application-dependent target functions while ensuring compatibility with existing fabrication processes. The results of the experimental characterization confirm the simulated tailored power distributions and optical efficiencies of the fabricated elements.

1. Introduction

Diffractive optical elements (DOEs) permit the generation of the spatial distribution of light beams by using a single element, and they are used for a variety of applications due to their high design flexibility, compact size, and mass productivity. For instance, diffractive beam splitters, often also referred to as fan-out gratings, have various applications, ranging from optical interconnects [1], multifocal microscopy [2,3], camera calibration [4], optical system distortion measurement [5] to structured light projectors [6,7]. For many applications, the goal is to propagate all the light in the desired orders and avoid losses. Nowadays, DOEs generating wide-angle spot arrays are used in a promising field of applications [7–9] with recent developments in fabrication technology realizing nanoscale features.

As long as only small to moderate diffraction angles are required, the iterative Fourier transform algorithm (IFTA) [10–12] based on the thin element approximation (TEA) [13] is widely and successfully used for the design of the microstructure surface of the DOEs. However, when larger angles are required, this approach suffers from several severe shortcomings and effectively gets unusable. Among those shortcomings, the limited choice of diffraction angles and the geometric distortions can be corrected for most easily, and IFTA's computation scheme can be still be used with moderate extensions and modifications [14,15]. A significantly more severe problem is the insufficient modeling of the light field transmission through the DOE by the TEA [16,17]. A precise modeling can be obtained by rigorous electromagnetic diffraction theory, such as rigorous coupled-wave analysis (RCWA) [18–20]. This significantly increases the computation time, triggering efforts to improve the computation speed [21] and to find faster alternatives with similar accuracy [22]. However, for iterative computations schemes, a projection operator in the DOE domain for the far-field-adapted and back-propagated field is required, but cannot be derived in a similar manner using the rigorous electromagnetic methods.

To resolve this, some groups employed genetic algorithms or gradient-based algorithms based on the finite-difference time-domain (FDTD) method to optimize the DOEs [23–25]. FDTD requires high computational effort and thus have been applied only to the one-dimensional domain. Parametric optimization is another option and was used for design and analysis of only two-dimensional (2D) fan-out DOEs with low complexity, e.g., 3×3 array beam splitters [26]. The correspondingly significantly larger number of parameters poses a practical limitation to parametric optimization for those scenarios due to resulting very large computational efforts also, even if such microstructures and corresponding initial parameters can be found at all.

Other design approaches recently combined a genetic algorithm with the RCWA method to design large-angle 2D fan-out DOEs [27,28]. The experimental results of the fabricated DOEs verified the method is reliable, but the improvements were comparatively insignificant during the optimization so that the obtained elements still have a rather low performance with respect to uniformity error. Data-driven photonics inverse design approaches have also been investigated for binary fan-out DOEs in the non-paraxial domain, but again only for elements with low complexity [29]. In recent years, inverse design methods using the adjoint variable method [30–37], have attracted attention due to their successful application to the optimization of photonic devices. In the adjoint method, one can calculate the gradient with respect to a figure of merit based on only two rigorous simulations, no matter how many design parameters are utilized to describe the device. This approach resolves the mentioned problem of the missing projection operator for computational schemes in the non-paraxial domain. However, to the best of our knowledge, high-performance 2D fan-out DOEs with large diffraction angles have not been previously realized using inverse design. For example, the metagratings which are one kind of optical metasurfaces [38] have been developed extreme beam manipulation, while this design platform focused on manipulation of one or a few diffractions orders such as beam deflectors [39,40], not fan-out elements.

Here, we introduce a design approach for wide-angle DOEs, yielding very significant improvements in the uniformity of the created patterns while maintaining the total diffraction efficiency in target orders. We have focused our efforts to designing binary (i.e., 2-level) microstructures, because they are most easy to fabricate and thus obviously are very attractive for optical systems. A schematic of DOE generating 7×7 spot array is shown in Fig. 1(a). In order to obtain a start condition for our optimization, a 7×7 diffractive fan-out DOE is designed by TEA-based IFTA. Not surprisingly, the performance of this initial wide-angle
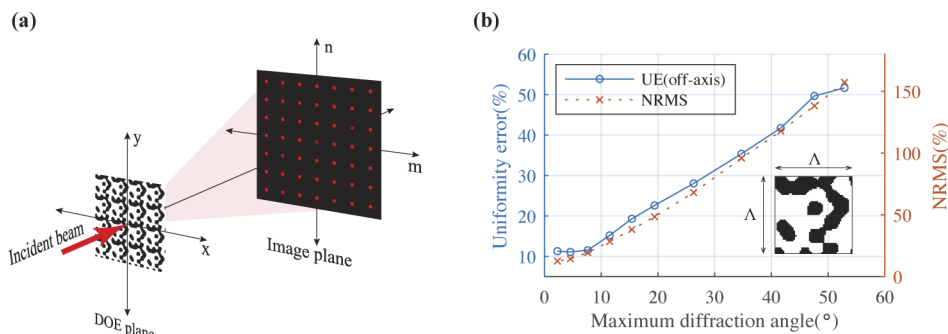

Fig. 1. (a) Scheme of two-dimension diffractive beam splitter generating 7×7 spot array. (b) Uniformity of 7×7 diffractive beam splitter designed by TEA-based IFTA as a function of maximum diffraction angle when the grating period Λ decreases. The Uniformity error and NRMS calculated using Eq. (9) and (10). The insets show the layout of the single unit cell. Black represents dielectric material and white represents air. The maximum angle is at $(3, 3)^{\text{th}}$ diffracted beam and the grating's normal vector.

fan-out DOE is very unsatisfactory with respect to uniformity (see Fig. 1(b)). We then apply to optimize large-angle 7×7 diffractive beam splitter but also beam splitter generating 7×5 non-square array spots. Beam-splitters creating equal intensity distribution are commonly used to various cases, while some applications potentially require fan-out DOE with various intensity distributions, for instance, vignetting correction [41]. Using our optimization method, we can create tailored-power-level beam splitters meeting the application's requirement. We measured the performance of fabricated samples based on the optimized designs and compared to calculated diffraction efficiency using RCWA simulation. Based on this analysis, we showed the robustness of our designs against fabrication errors and their suitability for high-quality optical systems.

2. Inverse design of wide-angle DOEs

Despite the advancement in lithography technologies, high cost and fabrication errors are inevitable for the fabrication of multilevel gratings. Thus, we focus on designing binary DOEs. Figure 2(a) shows a 2D binary grating profile characterized by depth, grating period, and distribution of relative permittivities. The binary gratings consist of pixels of relative permittivities corresponding to air (ϵ_1) or dielectric material (ϵ_2). The substrate layer (Layer I) is a dielectric material and the top layer (Layer III) is air. The permittivity distribution $\epsilon(\mathbf{r})$ in a single grating period (Layer II) is the design variables of the optimization procedure. Electromagnetic field distribution inside the grating can be obtained by RCWA solver [42,43]. High accuracy of the calculation in the desired diffraction channels is achieved when enough modes [20] are included in the calculation. To evaluate the accuracy of our numerical results, we analyze the convergence of simulation in our grating generating 7×7 spot array from the main text with incrementally increasing the number of Fourier modes. This defines the set of Fourier harmonics retained in x and y-axis from $-N$ to N, respectively. When N is large enough (e.g., $N>10$), all of the simulations converge to within 1 % of same value. To obtain accurate converged calculation, we thus use this value for the optimization process and final calculation of optimized devices reproduces with a higher number of modes $N = 25$. All theoretical results presented in this study show equivalent numerical accuracies.
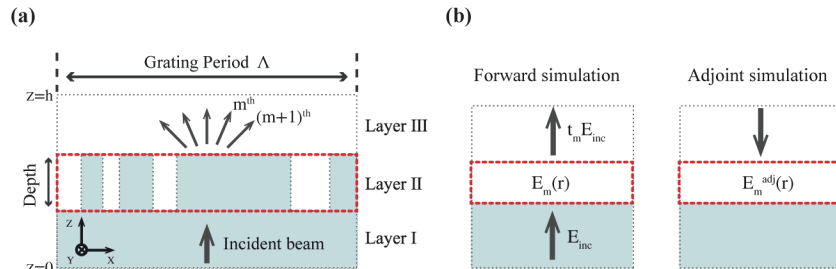

Fig. 2. (a) The surface profile of a grating structure in a single period. (b) Schematic of the forward and adjoint simulations in RCWA.

To design DOEs creating diffraction pattern with uniform and tailored-intensity-level distribution, we use the following figure of merit (FOM):

$$F = \sum_{m=-M}^{M} (\eta_m - \eta_{\text{obj}})^2 \tag{1}$$

where F represents the difference between the calculated diffraction efficiency η_m and the target diffraction efficiency η_{obj} in diffraction orders. The gradient of the FOM with respect to permittivity distribution $\epsilon(\mathbf{r})$ is crucial in determining the search direction to optima. For

instance, if the total pixel number K is large, it may easily become computationally heavy to calculate the gradient by RCWA analysis. The adjoint method, however, allows computing the variation for a diffraction efficiency by only two rigorous simulations, no matter how many pixels are present. The diffraction efficiencies η can be obtained by transmitted power flow going to the diffraction order represented by plane wave $\mathbf{E}, \mathbf{H}$:

$$
\begin{aligned}
\eta &= |t|^2 \\
&= \frac{1}{4\,|\Lambda|^2} \left| \int_\Lambda \left[\mathbf{E}(r') \times \mathbf{H_i^-}(r') - \mathbf{E_i^-}(r') \times \mathbf{H}(r') \right] \cdot \mathbf{n_z}\, dr' \right|^2
\end{aligned}
\tag{2}
$$

where both fields are evaluated at location $\mathbf{r}'$ on the $z = h$ plane above the grating and the overlap integral is performed for a single grating period. For the sake of simplicity, we assume the permittivity distribution does not depend on y-axis. The k-vector of $\mathbf{E_i}, \mathbf{H_i}$ is $(k_x, 0, k_z)$ and k-vector of $\mathbf{E_i^-}, \mathbf{H_i^-}$ is $(-k_x, 0, -k_z)$ and and transmitted amplitude t_m is normalized by $\frac{1}{2} \left| (\mathbf{E_i} \times \mathbf{H_i^-} - \mathbf{E_i^-} \times \mathbf{H_i}) \cdot \mathbf{n_z} \right| = 1$, where $\mathbf{n_z}$ is unit vector along z-axis. According to Eq. (13) and (14) in the Appendix, the change of η for a small perturbation in permittivity $\Delta\epsilon$ at a location r in the grating layer is given by:

$$
\Delta\eta = \frac{1}{|\Lambda|} \Re \left\{ t^* \int_\Lambda \left[\Delta E(r') \times H_i^-(r') - E_i^-(r') \times \Delta H(r') \right] \cdot n_z dr' \right\}
\tag{3}
$$

Using Eq. (15) and (16) in the Appendix, the derivative of diffraction efficiency with respect to permittivity is

$$
\frac{\partial\eta}{\partial\epsilon(r)} = \frac{1}{|\Lambda|} \Re \left\{ t^* \int_\Lambda \left[\hat{G}_{EP}(r',r)E(r) \times H_i^-(r') - E_i^-(r') \times \hat{G}_{HP}(r',r)E(r) \right] \cdot n_z dr' \right\}
\tag{4}
$$

Applying the triple product rule of vector identities and reciprocity of Green's tensor in Eq. (17) in the Appendix, we obtain the adjoint field:

$$
\begin{aligned}
\frac{\partial\eta}{\partial\epsilon(r)} &= \frac{1}{|\Lambda|} \Re \left(t^* \int_\Lambda \left\{ \hat{G}_{EP}(r,r') \left[H_i^-(r') \times n_z \right] \right. \right. \\
&\qquad \left. \left. - \hat{G}_{EM}(r,r') \left[E_i^-(r') \times n_z \right] \right\} dr \cdot E(r) \right) \\
&= \frac{1}{|\Lambda|} \Re \left[t^* E_{adj}(r) \cdot E(r) \right]
\end{aligned}
\tag{5}
$$

where adjoint field $\mathbf{E_{adj}}(\mathbf{r}) = \int_\Lambda \left\{ \hat{G}_{EP}(r,r') \left[H_i^-(r') \times n_z \right] - \hat{G}_{EM}(r,r') \left[E_i^-(r') \times n_z \right] \right\} dr'$ can be obtained by an solution of Maxwell's equation with illumination condition which is a plane wave generated by the polarization $(H_i^-(r') \times n_z)$ and magnetization densities $(E_i^-(r') \times n_z)$ from dipole expression. where the adjoint field $\mathbf{E_{adj}}(\mathbf{r})$ can be obtained by an auxiliary RCWA simulation. The Eq. (5) shows that one requires the derivative of diffraction efficiency from only two simulations, one direct $\mathbf{E}(\mathbf{r})$ and adjoint $\mathbf{E_{adj}}(\mathbf{r})$ to evaluate the derivatives for all pixels. In other words, a very large number of design parameters can be adjusted simultaneously, and the adjoint method unlocks the possibility to optimize particularly complex structures such as wide-angle DOEs with a much lower computational cost.

We employ spatial filtering [44] and projection function [45] during the optimization. We discuss our method for driving the dielectric continuum to discrete values of dielectric material and air and maintaining the fabricable minimum feature size over the iterative process. For the optimization, the starting point is a structure designed IFTA with applying a spatial filter to generate the dielectric continuum. We update a design density ρ which have a value from 0 to

1, rather than updating the permittivity distribution ϵ directly (see Fig. 3(a)). For generating a structure with larger feature sizes, a spatial loss-pass filter can be applied to ρ to create a filtered density $\tilde{\rho}$:

$$\tilde{\rho}_i = \frac{\sum_{j \in \mathbb{N}_i} W_{ij} \rho_j}{\sum_{j \in \mathbb{N}_i} W_{ij}} \tag{6}$$

where $\mathbb{N}_i$ denotes the design region, and W_{ij} is the weighting matrix, defined for a blurring radius of R as

$$W_{ij} = R - |r_i - r_j| \tag{7}$$

with $|r_i - r_j|$ being the distance between pixel i and j. This defines a spatial filter on ρ with the effect of smoothing out features with a length scale below R. The effect of this filter with 300 nm radius of R on a sample design density distribution is illustrated in Fig. 3(b). The filtered geometry becomes then a binary pattern using projection function. We define $\bar{\tilde{\rho}}$ as the projected density, which is created from blurred density $\tilde{\rho}$ as

$$\bar{\tilde{\rho}}_i = \frac{\tanh(\beta\gamma) + \tanh(\beta[\tilde{\rho}_i - \gamma])}{\tanh(\beta\gamma) + \tanh(\beta[1 - \gamma])} \tag{8}$$

where a threshold factor γ between 0 and 1 which controls the threshold of the projection, typically 0.5, and β controls the strength of the projection, bigger value delivers harder binarization. The projected density distribution in Fig. 3(c) is recreated from blurred pattern in Fig. 3(b) with $\gamma = 0.5$ and $\beta = 300$. We also observe that the combination of circular spatial blurring filter and projection function can remove tiny features. The final relative permittivity distribution from the projected pattern is shown in Fig. 3(d). In addition, we can describe an analytical solution of the determination of $\frac{\partial\epsilon}{\partial\bar{\tilde{\rho}}}$, $\frac{\partial\bar{\tilde{\rho}}}{\partial\tilde{\rho}}$, $\frac{\partial\tilde{\rho}}{\partial\rho}$ [45], these filters can be combined with the derivatives of figure of merit calculated by adjoint method. The obtained gradient was used in optimization based on the limited-memory Broyden-Fletcher-Goldfarb-Shanno (L-BFGS) algorithm [46,47].
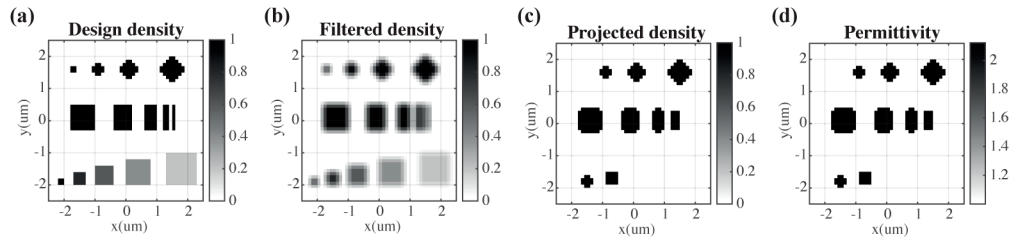

Fig. 3. Filtering and projection of an example design density. (a) the initial design density ρ before processing. (b) the density after applying the spatial filter, $\tilde{\rho}$. (c) the density after applying projection, $\bar{\tilde{\rho}}$. (d) the final relative permittivity ϵ.

In these filter and projection functions, we can control the strength of the projection so that the binary structure is gradually obtained by updating the strength factor over several iterations during the optimization process. The optimization is performed in an iterative approach and typically $100 - 200$ iterations are used to achieve convergence. The starting points in gradient optimization are designs from IFTA optimizations with applied spatial filter and projection function.

3. Simulation results

Two kinds of 2D fan-out gratings were selected for verification of the proposed design approach. The first one is a common multi-spot generator which creates a 7×7 array of spots with equal intensity distribution, and the other generates a two-dimensional array of spots with the designated

intensity distribution. To evaluate DOEs with various diffraction efficiency distribution, we define uniformity error (UE) and normalized root-mean-square error (NRMS) σ as follows:

$$UE = \frac{\tilde{\eta}_{\max} - \tilde{\eta}_{\min}}{\tilde{\eta}_{\max} + \tilde{\eta}_{\min}} \tag{9}$$

$$\sigma = \sqrt{\frac{1}{MN} \sum (\tilde{\eta}_{m,n} - \tilde{\eta}_{\mathrm{obj}})^2} \tag{10}$$

where $\tilde{\eta}_{\max}$ and $\tilde{\eta}_{\min}$ represent the maximal and minimum intensity of the relative diffraction efficiency $\tilde{\eta} = \frac{\eta}{\eta_{\mathrm{obj}}}$,respectively. The $\eta_{m,n}$ is the diffraction efficiency in orders on 2D array and M, N is the total number of diffraction orders along horizontal and vertical axis, respectively (see Fig. 1(a)). The target diffraction efficiency distributions $\eta_{\mathrm{obj}} \in [0, 1]^{m \times n}$ have uniform or specific entries. The spot energy distribution can be designed for any distribution meeting the application's requirements. The NRMS with scaled diffraction efficiency $\tilde{\eta}$ is preferable to with normal diffraction efficiency η because scaled diffraction efficiency facilitates the comparison among various diffraction efficiency distributions with different scales from diverse DOEs. Lower values of both UE and NRMS indicate less residual variance so that our objective is to minimize UE and NRMS of a DOE design given certain diffraction efficiency distribution. The fused silica (SiO$_2$) was selected as a material for DOE. The refractive index of SiO$_2$ is assumed as $n_2 = 1.45$. Transverse electric (TE) polarized (i.e., electric field component along the y-axis, see Fig. 2(a) for the coordinate system) monochromatic light with a wavelength of $\lambda = 940$ nm is incident wave from the substrate side with normal incidence angle. We selected incident beam with TE polarization, but beam splitters can be optimized also for transverse magnetic (TM) polarization or both TE and TM polarization. In general, the diffracted beam through gratings has both TE and TM polaization, the diffraction efficiency is the sum of efficiencies of both TE and TM polarization. The grating period is 5 µm×5 µm and the pixel size is 100 nm×100 nm. The depth of the grating was selected as $d = 1.18$ µm. Thus, the maximal diffraction angles of 7×7 and 7×5 diffractive beam splitter are about $53°$ at $(3, 3)^{\mathrm{th}}$ order and $43°$ at $(2, 3)^{\mathrm{th}}$ order from $(0, 0)^{\mathrm{th}}$ order, respectively.

3.1. Diffractive beam splitter with uniform intensity distribution

To optimize this 7×7 diffractive beam splitter, we define our figure of merit as Eq. (1) with the uniform intensity distribution of target efficiency η_{obj} and find the local optima using L-BFGS with the gradient calculated by the adjoint method. The objective of this design process is to create the grating structure which can accurately diffract the incident light into 49 in different directions with equal intensity distribution. Figure 4(a) and 4(b) show the merit function as a function of the optimization iterations of 7×7 and 7×5 diffractive beam splitters. To minimize the modifications of the adjoint sensitivity, the projection strength factor incrementally increases every 10 iterations for binarization. This function results in immediate effects in the figure of merit, which can be visualized as disconnections on the dash lines. The figure of merit converged well and the algorithm found the optimum point after 80 iterations in both cases. The simulated diffraction efficiency distributions of DOEs before and after optimization is shown in Fig. 4(a) and 4(b). These results are calculated for normally incident TE polarized light, i.e., the electric field component along the y-axis.

In the diffraction pattern, the maximal diffraction angle is about $53°$ at $(3, 3)^{\mathrm{th}}$ order spot from the center. For an accurate comparison, we calculated the total diffraction efficiency, UE, and NRMS of two different situations of two diffractive beam splitters: Initial and optimized. The total diffraction efficiency of 49 spots of initial and optimized 7×7 spot-array generators are 79.96 %, and 79.71 %, respectively. This optimized element thus has no degradation in total diffraction efficiency while there is considerable improvement in UE from 63.79% to 16.35% and
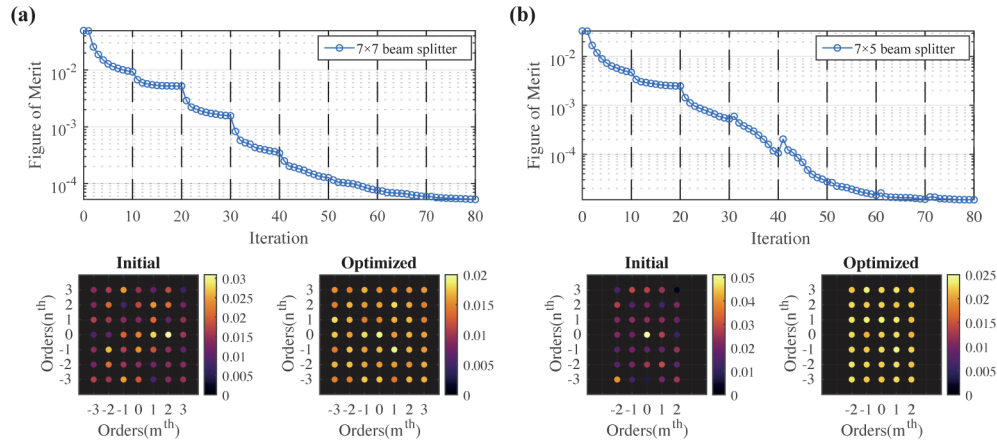
Fig. 4. Theoretical analysis of large-angle diffractive beam splitters. Plots of the figure of merit over the course of the optimization process of 7×7 (a) and 7×5 (b) diffractive beam splitter. In the bottom figures, the calculated efficiency of diffractive beam splitter before and after optimization.

NRMS from 32.62% to 7.74%, through adjoint-based optimization. In this optimized element, the remnant optical power goes in to reflection 9.38% and undesired orders 10.91% of incident power. Over optimization process, 7×5 spot-array generator also has significant improvement in UE from 81.1% to 6.98% and NRMS from 37.93% to 3.78%. Moreover, the total diffraction efficiency of 35 spots created by this DOE slightly increases from 74.45% to 78.48%. By comparison, H. Hao *et al*. [27] noted that they achieved 17.4 % of uniformity error and 71.4 % of total efficiency in 5×5 beam splitter with maximal 35° of diffraction angle using a genetic algorithm which is one kind of meta-heuristic optimization often required high computation cost. Thus the gradient-based optimization with adjoint-state-method, with much lower computational cost, be able to yield better results, i.e., better uniformity, higher efficiency, and larger angle, than optimization based on genetic algorithm.

3.2. Diffractive beam splitter with tailored intensity distribution

Furthermore, we applied our optimization method to the diffractive beam splitter with tailored power distribution corresponding to Fig. 5. As listed in Table 1, we specify different 9 groups have spot array with a specific intensity ratio, where group A, B, C, D, E, B', C', D' and E' have 1.0, 1.5, 2.0, 2.5, 1.0, 1.5, 2.0, 2.5 and 1.0 of intensity ratio, respectively.

To optimize this diffractive beam splitter, we also use the figure of merit function in Eq. (1) with target efficiency distribution of above entries (see Table 1). Over the course of multiple iterations, the dielectric continuum in the device converges to the dielectric constant of either silica or air from initial dielectric distribution designed by IFTA. We finally obtain a diffraction pattern distribution of optimized design nearly identical to the target pattern. The optimization convergence and pattern distribution before and after optimization are shown in the Fig. 6. The optimization process is performed iteratively and typically takes $100 - 200$ iterations to achieve convergence. Figure 6(a) shows the merit function as a function of the optimization iterations for beam-splitter generating the tailored spot array in the main text. The dash lines indicate the updating of projection strength β. The bottoms figures present the patterns in a single period of the device at different stages of the process. The simulated diffraction efficiency distributions of DOEs after optimization is shown in Fig. 6(b). Quantitatively, total efficiency of this DOE slightly increases from 75.20 % to 78.28 % and UE and NRMS consequently reach 8.45 % from

74.73 % and 4.14 % from 55.15 %. These results prove that the optimization algorithm is suitable for designing wide-angle diffractive beam splitters with various shapes of spot array and intensity distributions. For instance, proposed optimization strategy can be also used for even number fan-out beam splitters, with a zero intensity in zero-th order. Based on optimized designs, we fabricated and characterized diffractive beam-splitters. The details of experimental results are presented in the following section.
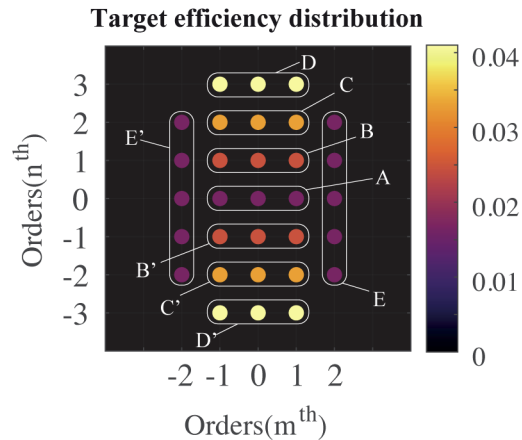

Fig. 5. The target diffraction pattern for diffractive beam splitter with designated intensity distribution. The target efficiency depends on the groups, where group A, B, C, D, E, B', C', D' and E' have 1.0, 1.5, 2.0, 2.5, 1.0, 1.5, 2.0, 2.5 and 1.0 of intensity ratio, respectively. (see Table 1)

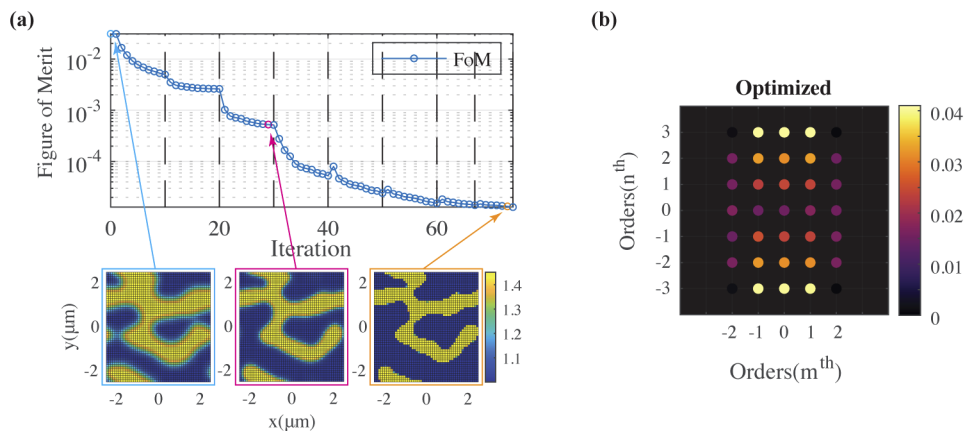**Fig. 6.** Theoretical analysis of diffractive beam splitters generating the tailored spot array. (a) a plot of the figure of merit over the course of the optimization process for the beam splitter with tailored intensity distribution. The bottoms figures show refractive indices distributions of the device at different stages of the optimization process. (b) the calculated efficiency of diffractive beam splitter after optimization.

Table 1. The target efficiency depends on groups in beam splitter with the tailored intensity distribution

Groups	A	B	C	D	E
		B'	C'	D'	E'
Efficiency ratio	1.0	1.5	2.0	2.5	1.0
Target efficiency (%)	1.63	2.45	3.27	4.08	1.63

4. Experimental results

The diffractive beam splitters were fabricated by lithography using electron-beam and dry etching to create a chromium etch mask, and then by reactive ion etching to obtain SiO_2 binary surface relief structures. The optical elements are optically characterized using a TE polarized 940 nm wavelength beam as our input source. We detect the diffracted light beams using a mobile single-pixel detector with a high dynamic range. To focus of both the simulation and experiment to facilitate a quantitative comparison, we applied the loss by Fresnel reflection from the interface between air and SiO_2 substrate to simulated efficiency of DOEs. The comparison between theoretical and experimental diffraction efficiencies of 7×7 and 7×5 beam-splitter creating uniform intensity array is presented in Table 2. The experimental data show that the DOEs operates with high-performance of uniformity. Total diffraction efficiency of of 7×7 and 7×5 beam splitters are calculated to 77.01% and 75.83%, respectively.

Table 2. Comparison with the theoretical and experimental properties of the 7×7 and 7×5 beam splitters. The calculated efficiency takes into account the loss from Fresnel reflection in the air-SiO_2 substrate interface.

	7×7 beam splitter		7×5 beam splitter	
	Calculated	Measured	Calculated	Measured
Diffraction efficiency (%)	77.01	75.35	75.83	73.86
UE (%)	16.35	23.35	06.98	14.42
NRMS (%)	08.35	12.76	06.10	10.50

The UE of 7×7 and 7×5 beam splitters are measured to 23.35% and 14.42%, respectively, which is close to the calculated values. In addition, excellent agreements in NRMS values of the DOEs are observed between the simulation and the measurement. Little discrepancies between the simulated and experimental efficiencies are due in part to minor geometric imperfections in the fabricated samples.

For an accurate comparison between theoretical and measured results, we analyze the correlation of these data using mean absolute percentage deviation (MAPD) as a ratio defined by the formula:

$$\text{MAPD} = \frac{1}{MN} \sum \left| \frac{\eta_{m,n}^S - \eta_{m,n}^E}{\eta_{m,n}^S} \right| \qquad (11)$$

where $\eta_{m,n}^S$, $\eta_{m,n}^E$ are simulated and experimental efficiency in $(m, n)^{\text{th}}$ diffraction orders and M, N is the total number of diffraction orders in two dimensional array. The MAPDs of 7×7 and 7×5 beam splitters are calculated to 7.24 % and 5.00 %, respectively, which represents measurements demonstrate excellent reproducibility of the simulated results in a quantitative manner.

We also measured the diffraction efficiency of tailored-intensity-level beam splitter fabricated based on optimized design. A scanning electron microscopy (SEM) image of the optical element is presented in Fig. 7(a), and theoretical and experimental diffraction efficiencies of the beam splitter with array groups and their objective efficiency are summarized in 7(b). Tilted SEM images of the beam-splitter show vertical sidewalls, indicative of high-quality etching. The

experimental plot shows that these elements operate with excellent agreement with respect to the objective in the overall intensity distributions. For an accurate comparison, we present the total diffraction efficiency, UE, and RMSE of simulated and measured one in Table 3. The UE and NRMS of the fabricated sample are measured to 14.54 % and 9.81 %, respectively. Moreover, the results of the comparison show that the experimental results have a strong correlation with the theoretical results, where the MAPD of this beam splitter is calculated to 5.99 %. The only noticeable deviation in the measurement is a small mismatch of diffraction efficiency in a few orders that emerge due to minor fabrication errors. In general the diffraction efficiency in orders often strongly depends on the errors in fabrication processes, e.g., etching depth, feature width, slope steepness, and feature rounding. Nevertheless, the fabricated samples based on optimized design overall display experimental performances which are significantly higher than the theoretical performances of initial designs before optimization. In other words, our methodology can readily create robust high-performance, multifunctional optical elements with wide-angle spot array that show theoretical and experimental performances that far exceed the previous record for manufacturable diffractive beam splitters recently reported [27–29], at much less computational cost than previous methods.
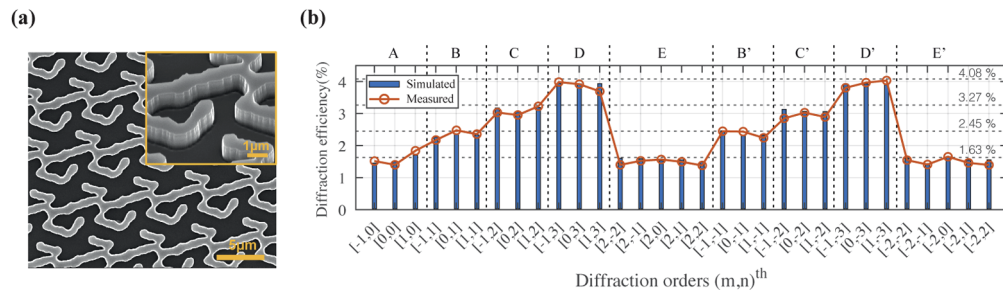

Fig. 7. Experimental characterization of the diffractive beam splitter with designated intensity distribution. (a) Scanning electron microscopy image of the diffractive beam splitter. Top insets: magnified tilted-view image of a grating unit cell. (b) The measured (orange line) and simulated (blue bar) efficiency of a beam splitter with tailored power distribution. The dash lines indicate the groups and their target efficiency

Table 3. Comparison with the simulated and experimental properties of the beam splitters with tailored power distribution. The simulated efficiency take into account the loss from Fresnel reflection in the air-SiO$_2$ substrate interface.

	Simulated	Measured
Diffraction efficiency (%)	75.63	74.20
UE (%)	08.46	14.54
NRMS (%)	06.57	09.81

5. Conclusion

In summary, we utilized the adjoint state method in optimizing the topology of optical elements, which is able to create high-performance, multifunctional wide-angle diffractive optical elements at a very low computational cost. We explored properties of the optimization method, such as efficient computation for the gradient of the target function with respect to high-dimensional design parameters with rigorous diffraction theory, and discussed the optimization method can readily extend to not only the diffraction beam splitter with equal intensity distribution but also DOE with the tailored intensity distribution. As a case study, we applied gradient-based

optimization with adjoint-state method to 7×7, 7×5 beam splitter and designated-power-level beam splitter with non-paraxial diffraction angle, i.e., maximal diffraction angle is $53°$, $43°$ and $37°$ from center, respectively. The optimized beam splitters show considerable improvement of uniformity while maintaining the initial diffraction efficiency. The experimental results obtained by the illumination of the fabricated optical elements using an incident laser of 940 nm wavelength with a normal incident angle have been compared with the numerical results. As numerical simulation and experimental results were found to be in excellent agreement, our optimization method can be considered proven to be an effective design tool for wide-angle diffractive beam splitters creating various diffraction distributions. We envision that these methods in diffractive optics will extend to other high-performance, multifunctional optical elements that will enable the next generation of photonics systems such as compact optical sensors.

Appendix

we can calculate electromagnetic field in isotropic medium from given illumination by using time-independent Maxwell's equation:

$$
\begin{aligned}
\nabla \times \boldsymbol{E} &= ik_0\mu(\boldsymbol{r})\boldsymbol{H} \\
\nabla \times \boldsymbol{H} &= -ik_0\epsilon(\boldsymbol{r})\boldsymbol{E}
\end{aligned}
\tag{12}
$$

where $\mu(\boldsymbol{r})$ and $\epsilon(\boldsymbol{r})$ is permeability and permittivity at location $\boldsymbol{r}$, respectively. For small perturbation in permeability and permittivity, the variation of electromagnetic field is the solution of following equations:

$$
\begin{aligned}
\nabla \times (\boldsymbol{E} + \Delta\boldsymbol{E}) &= ik_0\left[\mu(\boldsymbol{r}) + \Delta\mu(\boldsymbol{r})\right](\boldsymbol{H} + \Delta\boldsymbol{H}) \\
\nabla \times (\boldsymbol{H} + \Delta\boldsymbol{H}) &= -ik_0\left[\epsilon(\boldsymbol{r}) + \Delta\epsilon(\boldsymbol{r})\right](\boldsymbol{E} + \Delta\boldsymbol{E}).
\end{aligned}
\tag{13}
$$

We can simplify Eq. (13) by neglecting the $O(\Delta^2)$ terms so that equation becomes:

$$
\begin{aligned}
\nabla \times \Delta\boldsymbol{E} &= ik_0\left[\mu(\boldsymbol{r})\Delta\boldsymbol{H} + \Delta\mu(\boldsymbol{r})\boldsymbol{H}\right] \\
\nabla \times \Delta\boldsymbol{H} &= -ik_0\left[\epsilon(\boldsymbol{r})\Delta\boldsymbol{E} + \Delta\epsilon(\boldsymbol{r})\boldsymbol{E}\right]
\end{aligned}
\tag{14}
$$

which is a valid approximation if the change in the electromagnetic field from $\Delta\mu$ and $\Delta\epsilon$ is sufficiently small. The addition of this tiny perturbation $\Delta\mu$ and $\Delta\epsilon$ at location $\boldsymbol{r}$ can be treated as the dipole with polarization density $\boldsymbol{P}$ and a magnetization density $\boldsymbol{M}$ given by:

$$
\boldsymbol{P}(\boldsymbol{r}) = \Delta\epsilon(\boldsymbol{r})\boldsymbol{E}(\boldsymbol{r}) \qquad \boldsymbol{M}(\boldsymbol{r}) = \Delta\mu(\boldsymbol{r})\boldsymbol{H}(\boldsymbol{r})
\tag{15}
$$

By introducing Green's tensors, this dipole produces scattered fields to location $\boldsymbol{r}'$,which are described by:

$$
\begin{aligned}
\Delta\boldsymbol{E}(\boldsymbol{r}') &= \hat{\boldsymbol{G}}_{EP}(\boldsymbol{r}', \boldsymbol{r})\boldsymbol{P}(\boldsymbol{r}) + \hat{\boldsymbol{G}}_{EM}(\boldsymbol{r}', \boldsymbol{r})\boldsymbol{M}(\boldsymbol{r}) \\
\Delta\boldsymbol{H}(\boldsymbol{r}') &= \hat{\boldsymbol{G}}_{HP}(\boldsymbol{r}', \boldsymbol{r})\boldsymbol{P}(\boldsymbol{r}) + \hat{\boldsymbol{G}}_{HM}(\boldsymbol{r}', \boldsymbol{r})\boldsymbol{M}(\boldsymbol{r})
\end{aligned}
\tag{16}
$$

where $\boldsymbol{M}(\boldsymbol{r})$ terms can be omitted because $\Delta\mu(\boldsymbol{r}) = 0$ in our material. In addition, the Green's tensors in a reciprocal medium can be expressed by:

$$
\begin{aligned}
\hat{\boldsymbol{G}}_{EP}(\boldsymbol{r}', \boldsymbol{r}) &= \hat{\boldsymbol{G}}_{EP}(\boldsymbol{r}, \boldsymbol{r}') \\
\hat{\boldsymbol{G}}_{HP}(\boldsymbol{r}', \boldsymbol{r}) &= -\hat{\boldsymbol{G}}_{EM}(\boldsymbol{r}, \boldsymbol{r}').
\end{aligned}
\tag{17}
$$

Then we can drive the adjoint field using dipole representation and the Green's tensor expression above equations.

Funding

Acknowledgments

Disclosures

The authors declare no conflicts of interest.

References

1. D. F. Brosseau, F. Lacroix, M. H. Ayliffe, E. Bernier, B. Robertson, F. A. P. Tooley, D. V. Plant, and A. G. Kirk, "Design, implementation, and characterization of a kinematically aligned, cascaded spot- array generator for a modulator-based free-space optical interconnect," Appl. Opt. **39**(5), 733 (2000).
2. J. E. Jureller, H. Y. Kim, and N. F. Scherer, "Stochastic scanning multiphoton multifocal microscopy," Opt. Express **14**(8), 3406 (2006).
3. Z. Chen, B. Mc Larney, J. Rebling, X. L. Deán-Ben, Q. Zhou, S. Gottschalk, and D. Razansky, "High-Speed Large-Field Multifocal Illumination Fluorescence Microscopy," Laser Photonics Rev. **14**(1), 1900070 (2020).
4. M. Bauer, D. Griessbach, A. Hermerschmidt, S. Krüger, M. Scheele, and A. Schischmanow, "Geometrical camera calibration with diffractive optical elements," Opt. Express **16**(25), 20241–20248 (2008).
5. F. Wang, Z. Zhang, R. Wang, X. Zeng, X. Yang, S. Lv, F. Zhang, D. Xue, J. Yan, and X. Zhang, "Distortion measurement of optical system using phase diffractive beam splitter," Opt. Express **27**(21), 29803–29816 (2019).
6. R. Vandenhouten, A. Hermerschmidt, and R. Fiebelkorn, "Design and quality metrics of point patterns for coded structured light illumination with diffractive optical elements in optical 3D sensors," in *Digital Optical Technologies 2017*, vol. 10335 B. C. Kress and P. Schelkens, eds., International Society for Optics and Photonics (SPIE, 2017), pp. 264–276.
7. O. Barlev and M. A. Golub, "Multifunctional binary diffractive optical elements for structured light projectors," Opt. Express **26**(16), 21092 (2018).
8. S. Thibault, A. Arfaoui, and P. Desaulniers, "Cross-diffractive optical elements for wide angle geometric camera calibration," Opt. Lett. **36**(24), 4770 (2011).
9. P. Twardowski, B. Serio, V. Raulot, and M. Guilhem, "Three-dimensional shape measurement based on light patterns projection using diffractive optical elements," in *Micro-Optics 2010*, vol. 7716 H. Thienpont, P. V. Daele, J. Mohr, and H. Zappe, eds., International Society for Optics and Photonics (SPIE, 2010), pp. 704–711.
10. F. Wyrowski and O. Bryngdahl, "Iterative Fourier-transform algorithm applied to computer holography," J. Opt. Soc. Am. A **5**(7), 1058 (1988).
11. M. Skeren, I. Richter, and P. Fiala, "Iterative Fourier transform algorithm: comparison of various approaches," J. Mod. Opt. **49**(11), 1851–1870 (2002).
12. S. Bühling and F. Wyrowski, "Improved transmission design algorithms by utilizing variable-strength projections," J. Mod. Opt. **49**(11), 1871–1892 (2002).
13. J. W. Goodman, "Introduction to fourier optics," *Introduction to Fourier optics*, 3rd ed., by JW Goodman. (Roberts & Co. Publishers, Englewood, CO, 2005) 1 (2005).
14. A. Hermerschmidt, S. Krüger, and G. Wernicke, "Binary diffractive beam splitters with arbitrary diffraction angles," Opt. Lett. **32**(5), 448–450 (2007).
15. G.-N. Nguyen, K. Heggarty, A. Bacher, P.-J. Jakobs, D. Häringer, P. Gérard, P. Pfeiffer, and P. Meyrueis, "Iterative scalar nonparaxial algorithm for the design of fourier phase elements," Opt. Lett. **39**(19), 5551–5554 (2014).
16. D. A. Pommet, M. G. Moharam, and E. B. Grann, "Limits of scalar diffraction theory for diffractive phase elements," J. Opt. Soc. Am. A **11**(6), 1827 (1994).
17. T. Vallius, P. Vahimaa, and M. Honkanen, "Electromagnetic approach to the thin element approximation," J. Mod. Opt. **51**(14), 2079–2092 (2004).
18. P. Lalanne and G. M. Morris, "Highly improved convergence of the coupled-wave method for TM polarization," J. Opt. Soc. Am. A **13**(4), 779 (1996).
19. M. G. Moharam, E. B. Grann, D. A. Pommet, and T. K. Gaylord, "Formulation for stable and efficient implementation of the rigorous coupled-wave analysis of binary gratings," J. Opt. Soc. Am. A **12**(5), 1068–1076 (1995).
20. V. Liu and S. Fan, "S 4: A free electromagnetic solver for layered periodic structures," Comput. Phys. Commun. **183**(10), 2233–2244 (2012).
21. W. Iff, T. Kämpfe, Y. Jourlin, and A. V. Tishchenko, "Memory sparing fast scattering formalism for rigorous diffraction modeling," J. Opt. **19**(7), 075602 (2017).

22. A. Junker and K.-H. Brenner, "Achieving a high mode count in the exact electromagnetic simulation of diffractive optical elements," J. Opt. Soc. Am. A **35**(3), 377–385 (2018).

23. J. Jiang and G. Nordin, "A rigorous unidirectional method for designing finite aperture diffractive optical elements," Opt. Express **7**(6), 237 (2000).

24. M. E. Testorf and M. A. Fiddy, "Efficient optimization of diffractive optical elements based on rigorous diffraction models," J. Opt. Soc. Am. A **18**(11), 2908 (2001).

25. D. Feng, Y. Yan, G. Jin, and S. Fan, "Design and fabrication of continuous-profile diffractive micro-optical elements as a beam splitter," Appl. Opt. **43**(29), 5476–5480 (2004).

26. E. Noponen and J. Turunen, "Eigenmode method for electromagnetic synthesis of diffractive elements with three-dimensional profiles," J. Opt. Soc. Am. A **11**(9), 2494–2502 (1994).

27. H. Hao, Z. Tingting, S. Qiang, and Y. Xiaodong, "Wide angle 2D beam splitter design based on vector diffraction theory," Opt. Commun. **434**, 28–35 (2019).

28. G. Zhang, Q. Song, L. Wei, and X. Yin, "Inverse optimization for designing wide angle diffractive optical element," in *Eleventh International Conference on Information Optics and Photonics (CIOP 2019), H. Wang, ed.* (SPIE, 2019), December 2019, p. 117.

29. Z. Liu, Z. Zhu, and W. Cai, "Topological encoding method for data-driven photonics inverse design," Opt. Express **28**(4), 4825–4835 (2020).

30. C. M. Lalau-Keraly, S. Bhargava, O. D. Miller, and E. Yablonovitch, "Adjoint shape optimization applied to electromagnetic design," Opt. Express **21**(18), 21693 (2013).

31. A. Y. Piggott, J. Lu, K. G. Lagoudakis, J. Petykiewicz, T. M. Babinec, and J. Vučković, "Inverse design and demonstration of a compact and broadband on-chip wavelength demultiplexer," Nat. Photonics **9**(6), 374–377 (2015).

32. T. Hughes, G. Veronis, K. P. Wootton, R. Joel England, and S. Fan, "Method for computationally efficient design of dielectric laser accelerator structures," Opt. Express **25**(13), 15414 (2017).

33. J. Wang, Y. Shi, T. Hughes, Z. Zhao, and S. Fan, "Adjoint-based optimization of active nanophotonic devices," Opt. Express **26**(3), 3236 (2018).

34. Z. Lin, B. Groever, F. Capasso, A. W. Rodriguez, and M. Lončar, "Topology-Optimized Multilayered Metaoptics," Phys. Rev. Appl. **9**(4), 044030 (2018).

35. A. Michaels and E. Yablonovitch, "Leveraging continuous material averaging for inverse electromagnetic design," Opt. Express **26**(24), 31717 (2018).

36. S. Molesky, Z. Lin, A. Y. Piggott, W. Jin, J. Vuckovic, and A. W. Rodriguez, "Inverse design in nanophotonics," Nat. Photonics **12**(11), 659–670 (2018).

37. M. Mansouree, H. Kwon, E. Arbabi, A. McClung, A. Faraon, and A. Arbabi, "Multifunctional 2.5D metastructures enabled by adjoint optimization," Optica **7**(1), 77 (2020).

38. J. Sung, G.-Y. Lee, and B. Lee, "Progresses in the practical metasurface for holography and lens," Nanophotonics **8**(10), 1701–1718 (2019).

39. D. Sell, J. Yang, E. W. Wang, T. Phan, S. Doshay, and J. A. Fan, "Ultra-High-Efficiency Anomalous Refraction with Dielectric Metasurfaces," ACS Photonics **5**(6), 2402–2407 (2018).

40. J. Yang, D. Sell, and J. A. Fan, "Freeform Metagratings Based on Complex Light Scattering Dynamics for Extreme, High Efficiency Beam Steering," Ann. Phys. **530**(1), 1700302 (2018).

41. A. Kordecki, H. Palus, and A. Bal, "Practical vignetting correction method for digital camera with measurement of surface luminance distribution," Signal, Image Video Process. **10**(8), 1417–1424 (2016).

42. P. Lalanne and M. P. Jurek, "Computation of the near-field pattern with the coupled-wave method for transverse magnetic polarization," J. Mod. Opt. **45**(7), 1357–1374 (1998).

43. J.-P. Hugonin and P. Lalanne, *Reticolo software for grating analysis*, (Institut d'Optique, Orsay, France, 2005).

44. X. Qian and O. Sigmund, "Topological design of electromechanical actuators with robustness toward over- and under-etching," Comput. Methods Appl. Mech. Eng. **253**, 237–251 (2013).

45. F. Wang, B. S. Lazarov, and O. Sigmund, "On projection methods, convergence and robust formulations in topology optimization," Struct. Multidiscip. Optim. **43**(6), 767–784 (2011).

46. R. H. Byrd, P. Lu, J. Nocedal, and C. Zhu, "A Limited Memory Algorithm for Bound Constrained Optimization," SIAM J. on Sci. Comput. **16**(5), 1190–1208 (1995).

47. C. Zhu, R. H. Byrd, P. Lu, and J. Nocedal, "Algorithm 778: L-BFGS-B: Fortran subroutines for large-scale bound-constrained optimization," ACM Trans. Math. Softw. **23**(4), 550–560 (1997).